Structures of the bacterial ribosome in the classical and hybrid states of tRNA binding

Jack A. Dunkle, Leyi Wang, Michael B. Feldman, Arto Pulk, Vincent B. Chen, Gary J. Kapral, Jonas Noeske, Jane S. Richardson, Scott C. Blanchard and Jamie H. Doudna Cate

Supporting Online Material

Materials and Methods

Purification of native E. coli tRNA^{Phe}. The purification protocol for tRNA^{Phe} was adapted from a published protocol (*51*). Briefly, *Escherichia coli* (*E.coli*) cells (strain MRE600) harboring plasmid pBS-tRNA^{Phe}, which overexpresses *E.coli* tRNA^{Phe}, were cultured and harvested as previously described (*52*). The cell pellets were lysed by sonication in 20 mM Tris HCl pH=7.5, 50 mM $MgCl_2$ and 20 mM β-mercaptoethanol. The cell lysate was clarified by centrifugation at 35000 rpm in a Beckman Ti-70 rotor at 4°C for 2 hours. Total cellular RNA was extracted from the supernatant by phenol extraction and ethanol precipitation. High molecular weight RNAs were removed by isopropanol precipitation (*53*). The soluble RNA fraction was then incubated for 15 min at 37 °C after adjusting the pH to 8 by addition of 0.5 M Tris HCl pH=8.8 in order to deacylate tRNAs. As previously described (*54*), tRNA^{Phe} was specifically aminoacylated following brief incubation with phenylalanine, ATP and phenylalanyl-tRNA synthase. The reaction mixture was phenol extracted and the nucleic acid fraction was obtained

by ethanol precipitation. After resuspending the pellet in 10 mM ammonium acetate pH=6.3, the sample was applied to a TSK Phenyl 5PW hydrophobic interaction column (Tosoh Bioscience) and Phe-tRNA^{Phe} was purified by fractionation as previously described (*54*). The isolated peak was desalted, deacylated by brief incubation at elevated pH and repurified using analogous methods.

Ribosome recycling factor purification. RRF was purified from *E. coli* strain BL21 Star cells (Invitrogen) expressing a C-terminal hexa-histidine tagged version of the protein. Cells were lysed by sonication in lysis buffer (50 mM HEPES, pH=7.6, 1 M NH_4Cl, 10 mM $MgCl_2$, 200 μM PMSF, 7 mM β-mercaptoethanol, 0.1% Triton-X11, and Roche EDTA-free protease inhibitor cocktail). After the lysate was clarified by centrifugation, it was applied to a HisTrap column (GE Healthcare). The column was washed with buffer containing 50 mM HEPES, 1 M NH_4Cl, 10 mM $MgCl_2$, 7 mM β-mercaptoethanol, and 20 mM imidizole, and RRF was eluted in the same buffer containing 400 mM imidazole. The protein was concentrated by ultrafiltration and was applied to Sephacryl 16/60 size exclusion column (GE Healthcare). The RRF containing fractions were concentrated to 550 μM and stored at -80 °C.

Preparation of dye-labeled ribosome complexes. The labeling of L1 protein (Cy5-S55C) and tRNA^{Phe} (Cy3-s^{4}U8) for smFRET experiment were performed as previously described (*55*). 70S ribosome were reconstituted with dye-labeled L1 and non-enzymatically initiated with mRNA and (Cy3-s^{4}U8) tRNA^{Phe} by incubating with 1.5 molar excess of each over ribosomes at 37°C for 10 minutes. The mRNA used has the

same sequence as the one used in crystallization except for biotin modification at 5' end to enable surface immobilization.

Single-Molecule Fluorescence Experiments. All single-molecule fluorescence experiments were performed at room temperature in an MES-Polymix buffer that resembled the crystallization condition (50 mM MES, pH 6.5, 5.0 mM $MgCl_2$, 350 mM NH_4Cl, 5.0 mM putrescine, 5.0 mM spermidine, 5 mM β-mercaptoethanol and 0.5 mM EDTA). Oxygen scavenging and triplet-state quenching systems used were as previously described (*56*). The smFRET data were acquired with Metamorph (Molecular Device), and analyzed in MATLAB (Mathwork) and QuB (www.qub.buffalo.edu) as previously described (*55*). Subunit release was monitored by directly exciting the Cy5 fluorophore within surface-immobilized ribosome complexes (Coherent) at 10 mW laser power. Time lapse imaging of the recycling reaction was performed by acquiring snapshot images (40 millisecond integration time) every 20 seconds over the course of 20 minutes. Changes in fluorescence intensity were analyzed and plotted in Origin (OriginLab).

Ribosome purification and crystallization. Ribosomes lacking protein S1 were purified from *E. coli* strain MRE600 using sucrose gradient centrifugation, as described (*57*). Ribosomes were crystallized at 18 °C using microbatch 96-well plates and buffers containing 4.0-6.0% 2-methyl-2,4-pentanediol (MPD), 4.1-4.5% PEG 8000, 4.0 mM $MgCl_2$, 380 mM NH_4Cl, 5.7 mM putrescine, 5.0 mM spermidine, 10 mM Tris plus 40 mM MES, pH=6.5-7.0, and 0.25 mM EDTA. Ribosome complexes were formed by

incubating 4 μM deacylated $tRNA^{Phe}$ and 8 μM mRNA of sequence 5'-GGCAAG GAGGUAAAAUUCUACAAA-3' (Dharmacon) with 2 μM ribosomes at 37 °C for 15 minutes. 8 μM RRF was then added and the samples were incubated for an additional 15 minutes incubation at 37 °C. Prior to crystallization, samples were subjected to ultrafiltration to remove excess ligands.

Data collection and processing. Ribosome crystals were stabilized with crystallization buffer containing 7.0% MPD, 7.0% PEG 8000 and 24% PEG 400, pH=4.8, to allow cryocooling of the crystals to liquid nitrogen temperatures. Diffraction data were measured from crystals cooled to 100 K using 0.1-0.3° oscillations at beamlines 24ID-C at the Advanced Photon Source or at the Advanced Light Source (SIBYLS and 8.3.1 beamlines), each of which is equipped with an ADSC Q315 area detector. Data were reduced using XDS (*58*), yielding the statistics shown in Table S1.

Molecular replacement and structure refinement. The two copies of the 70S ribosome in the crystallographic asymmetric unit were located using rigid-body refinement in Phenix (*59*) of the well-ordered *E. coli* ribosome from a recent atomic-resolution structure determination (*8*). That starting model had previously been improved by diagnosing problems with stereochemistry, all-atom sterics, and conformations using MolProbity (*60*) and correcting them using a variety of protein and RNA remodeling tools. RNA corrections were carried out with the automated RNABC software (*61*), and were accepted if the fixes of all-atom clashes (*62*), ribose pucker outliers or backbone conformer outliers (*63*) survived in refinement without

compromising model geometry or R-factors. Protein corrections first included automated correction of Asn/Gln/His 180° "flips" (*64*) in MolProbity or Phenix. More extensive corrections were carried out in Coot (*65*) or with the backrub (*66*) and sidechain-rotator tools in KiNG (*67*). Refinement was carried out in Phenix, including the use of pucker-specific target parameters. Corrections made prior to this new structure included rebuilds of 20 RNA suites with RNABC, plus pucker corrections in refinement, and numerous improvements to 50S proteins (*68*), including sequence register-shifts, peptide flips in β-strands, and rotamer repairs of H-bonding at protein/RNA interfaces, to produce the model used in molecular replacement.

The resulting structural models were then refined using rounds of manual rebuilding in O (*69*), Coot, or KiNG as well as positional refinement in Phenix, including use of a new functionality for automatic assignment of H-bond restraints using the Saenger base-pair types (*70*). Electron density maps were generated from the Phenix output directly, or using the program Pirate (*71*). RNA rebuilding concentrated on the tRNAs and mRNAs, using the RNArotator tool in KiNG to make changes that improved both steric clashes and ribose pucker outliers in those regions to 80-90th percentile levels for this resolution. Protein corrections concentrated on RRF, L5, L27, and S12, in some cases making dramatic improvements such as taking L27 from a 0th percentile MolProbity score (combined clash, Ramachandran, and rotamer criteria) to 53rd percentile for the R_0 molecule and 88th percentile for the R_F molecule. While the overall sterics, geometry, and RNA conformations are all well above median quality (high percentile scores in Table S2), future rebuilding and refinements will be used to further

improve protein and RNA sterics and geometry. In contrast to the earlier *E. coli* 70S structure determination (*8*), in which one of the two molecules was partially disordered, both ribosomes in the present structure are well ordered, with similar B-factors, validation statistics, and electron density quality.

Least-squares superpositions. Comparisons to atomic-resolution structures of the ribosome, and to structural models of the intact ribosome refined against cryo-EM density maps, were carried out by least-squares superposition in the program O (*69*), using ribose C1' positions or phosphorous atoms in nucleotides. Superpositions to identify the relative position of the small and large subunits in the ribosome used the large subunit as the frame of reference (*37*). The angles of rotation of the 30S subunit domains were calculated essentially as described in (*8*). Angles given for the rotation of the head domain were calculated from 30S subunit structures superimposed by means of their platform domains. A rotation of 0° is defined as centering the head domain over the 30S P site, as seen in the structure of the unratcheted ribosome presented here. The bending angle of helix H34 in 23S rRNA, part of bridge B4, was determined from the shift in position of A715 relative to G725 at the based of the helix. Superpositions of P/E, P/P and A/T tRNAs utilized the C1' atoms of nucleotides 31-39 in the anticodon stem-loop. Comparisons of tRNA bending angles used the glycosidic bond of position 31 near the end of the anticodon stem-loop and the glycosidic bond of nucleotide 63 in the superimposed tRNAs. The bending angles calculated in this way are 37° for A/T

tRNA compared to P/P tRNA, 37° for P/P tRNA compared to P/E tRNA, and 70° for A/T tRNA compared to P/E tRNA.

Structurally conserved nucleotides in the yeast 80S ribosome were used for superpositions of the two yeast 80S ribosome structures (*11*) with the bacterial 30S and 50S subunits (Table S3). One of the yeast 80S ribosomes most closely aligns with the post-translocation state recently identified (*10*). The body and platform domains are not fully rotated, and the small subunit head domain is rotated towards the E site by ~16°. In the yeast 80S ribosome, H69 is extended, as seen in the unrotated state R_0 and the ratcheting intermediate R_2 (*8*), and is not compressed, as seen in the present structure of the fully rotated state R_F.

Intersubunit contacts. Contacts, or bridges, between the ribosomal subunits were determined using the program Probe (*62*). Identified contacts were manually examined by comparison to difference electron density maps, calculated either in Phenix or using Pirate density modified phases, to discount disordered side chains. Only direct contacts are shown in Figures 3 and S4. Nomenclature for bridges adapted from (*11, 25, 72*). The dinucleotide platform formed by nucleotides A1847-A1848 in 23S rRNA differs from prior structural models of the 70S ribosome (*19, 25, 73, 74*), although in *Haloarcula marismortui* the motif is conserved as a U-A dinucleotide platform (nts U1888-A1889)(*75*).

Figure preparation. Figures were made using the program Pymol (*76*). Numbering for ribosomal proteins follows that in the UniProt database (http://www.uniprot.org) (*77*). Morphing movies were made using interpolation scripts written for CNS (*78, 79*) and were rendered in Pymol (*76*).

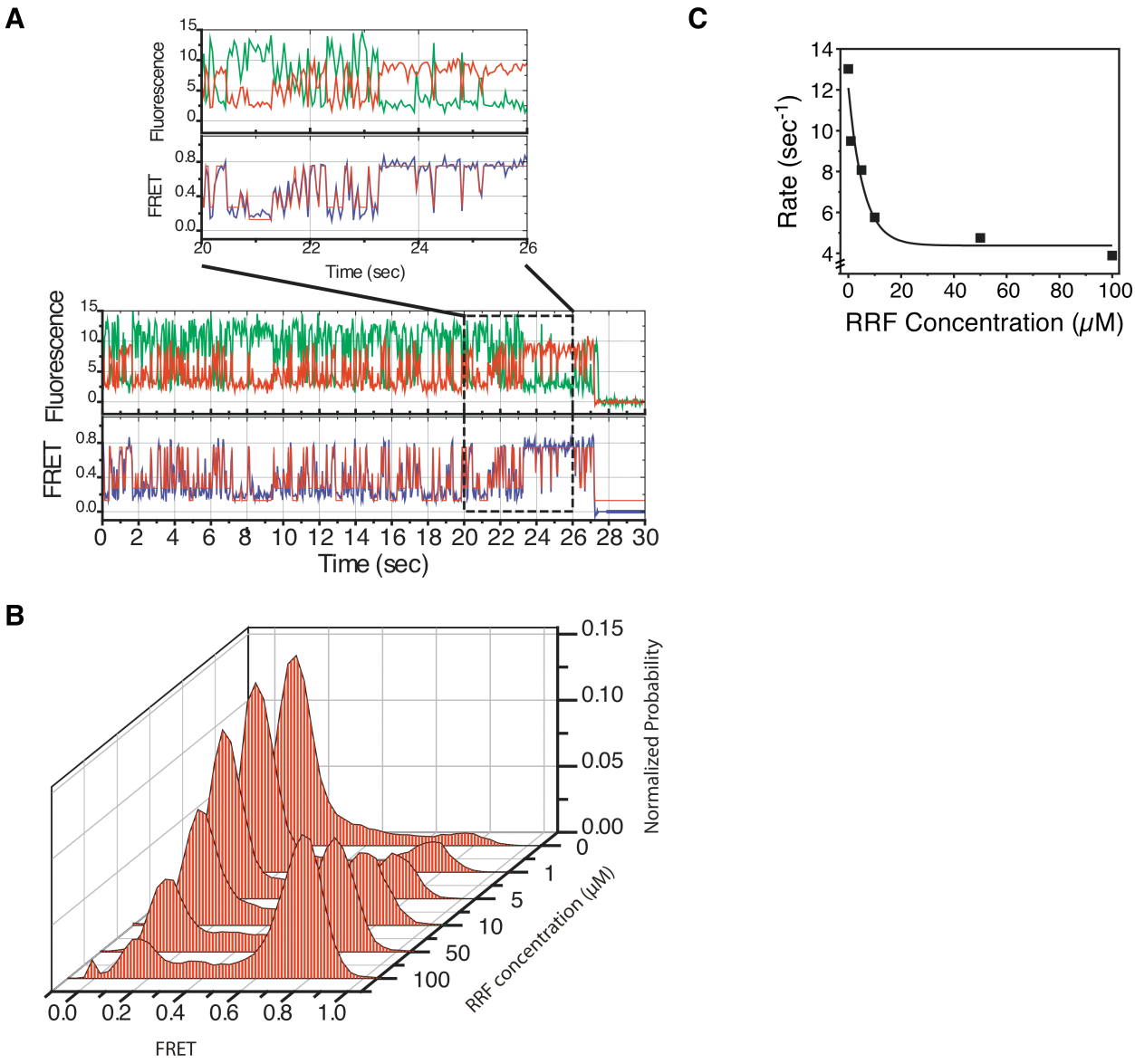

Figure S1. Dynamics between the L1 stalk and P-site $tRNA^{Phe}$. As previously reported (*55, 80*), complexes bearing (Cy5-S55C) L1 protein and (Cy3-s^4U8) $tRNA^{Phe}$ achieve a high-FRET state upon the simultaneous occurrence of hybrid state formation (P/E) and L1 stalk closure. (**A**) Representative single-molecule fluorescence (Cy3, green; Cy5, red) and FRET (blue) trajectories obtained from ribosome complex bearing Cy5 labeled deacylated P-site $tRNA^{Phe}$ and Cy3 labeled L1 protein, imaged at 40 millisecond time resolution at room temperature in buffer conditions resembling those used in

crystallographic experiments. Idealization of the smFRET trajectory, as previously described (*55*), is overlaid in red. The boxed region in the upper panel shows an expanded region of the smFRET trajectory. (**B**) Individual FRET trajectories summed into population FRET histograms to reveal changes in relative in the population with increasing RRF concentrations. (**C**) RRF-induced stabilization of the unlocked state of the ribosome (hybrid P/E tRNA; closed L1 stalk), detected by the decrease in transition rate out of a high-FRET state between Cy5-labeled protein L1 and Cy3-labeled P-site $tRNA^{Phe}$ (Fig. S1). The apparent K_d for RRF based on the decrease in the transition rate is 5.7 μM.

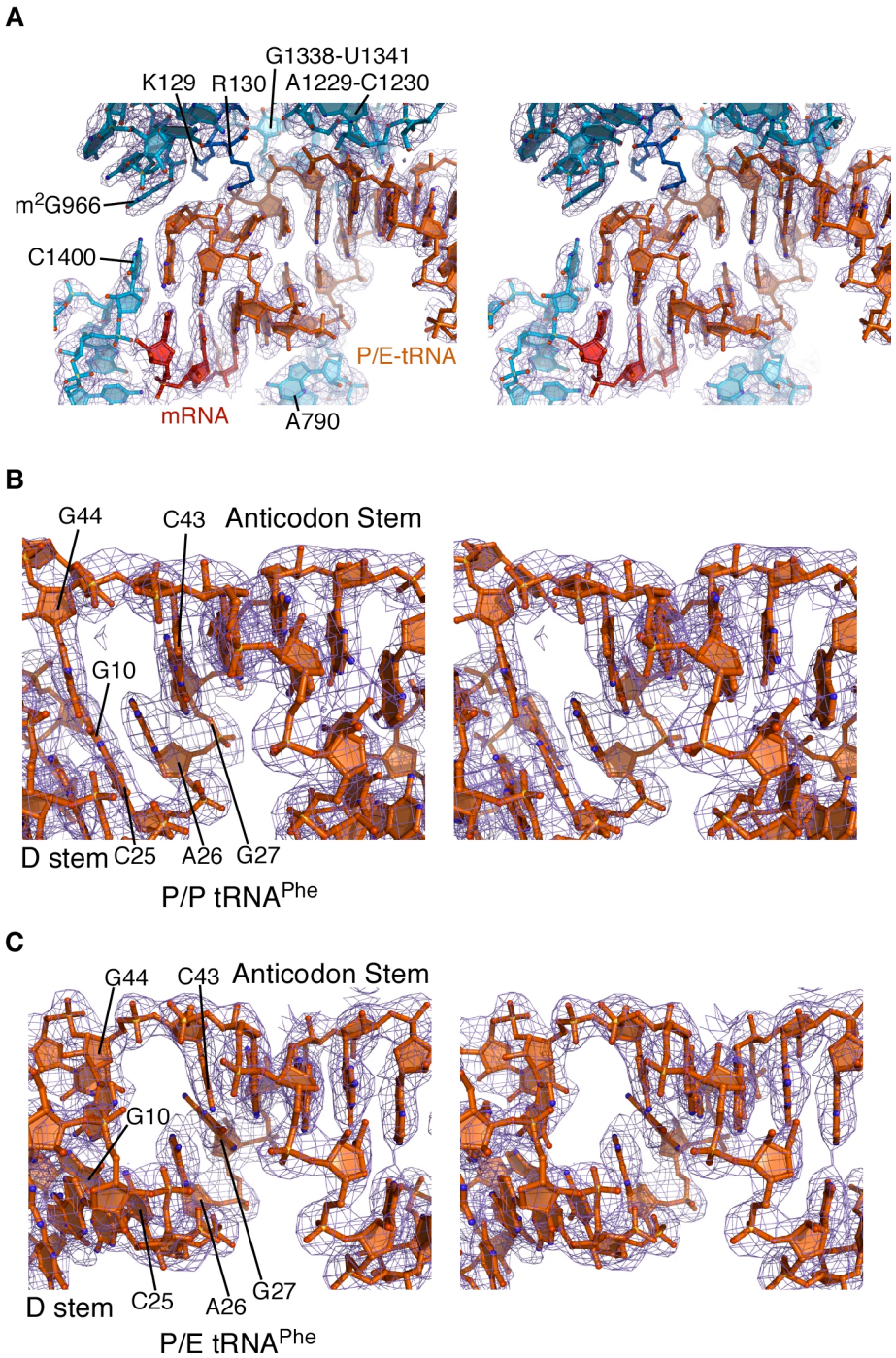

Figure S2. Stereo views of electron density maps for P/P tRNA and P/E tRNA. (**A**) Electron density map for the anticodon stem-loop region of P/E tRNA. Shown is a ($2F_{obs} – F_{calc}$) electron density map, calculated using sharpened amplitudes and Pirate

density-modified structure factor phases and contoured at 0.7 standard deviations from the mean. (**B**) Electron density map for P/P tRNA. Shown is a ($2F_{obs} – F_{calc}$) electron density map, calculated in Phenix and contoured at 1.1 standard deviations from the mean. The region shown is the junction between the anticodon stem, variable loop, and D stem. (**C**) Electron density map for P/E tRNA, as in B. In B and C, the base triple between G10, C25, and G44 in $tRNA^{Phe}$ in these structures is marked.

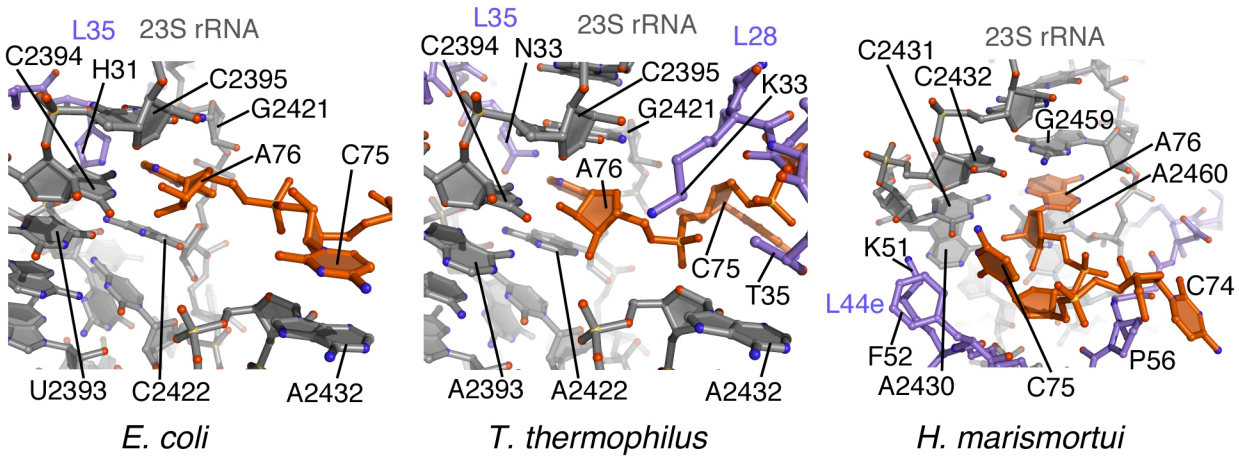

Figure S3. Interactions of the 3'-CCA end of P/E tRNA with the 50S subunit E site. Elements of 23S rRNA (grey), tRNA (orange) and ribosomal proteins (purple) are shown. *E. coli* numbering is used for nucleotides and amino acids for the left and middle panels. Numbering for *H. marismortui* is used in the right panel. The positions of proteins L35, L28, and L44e are marked.

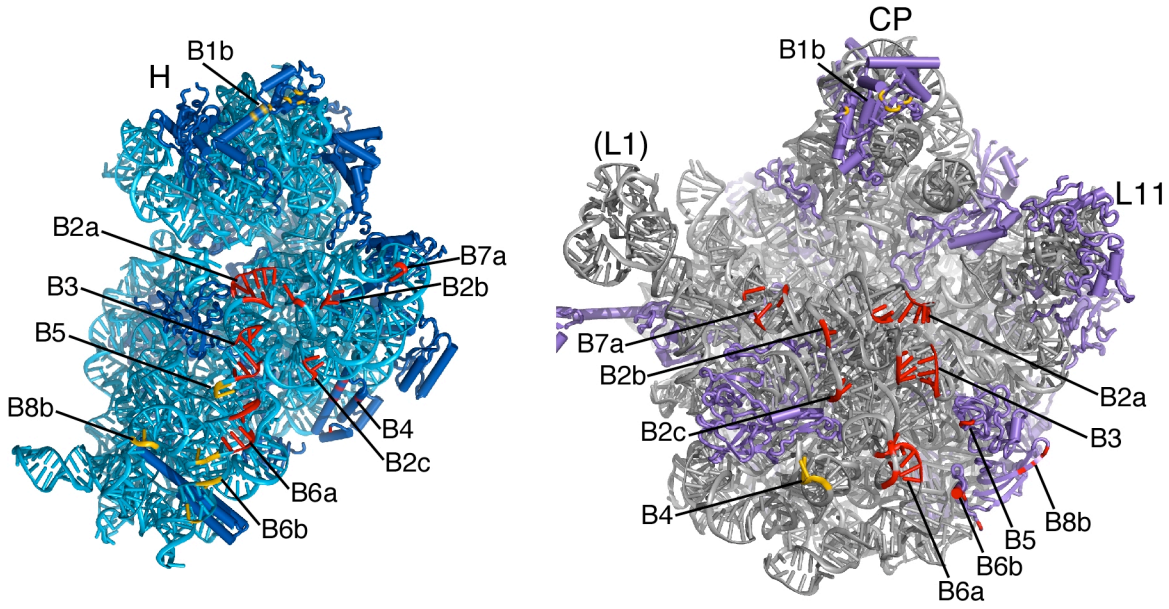

Figure S4. Bridges between the two ribosomal subunits in the unrotated state. Elements in each ribosomal subunit that contact rRNA in opposite subunit are color-coded red, while elements in each subunit that contact ribosomal proteins in the opposite subunit are color-coded gold. The small subunit rRNA and proteins are colored light and dark blue, respectively, with the large subunit rRNA and proteins colored grey and magenta, respectively. The tip of helix H38 in bridge B1a is disordered in the present structures.

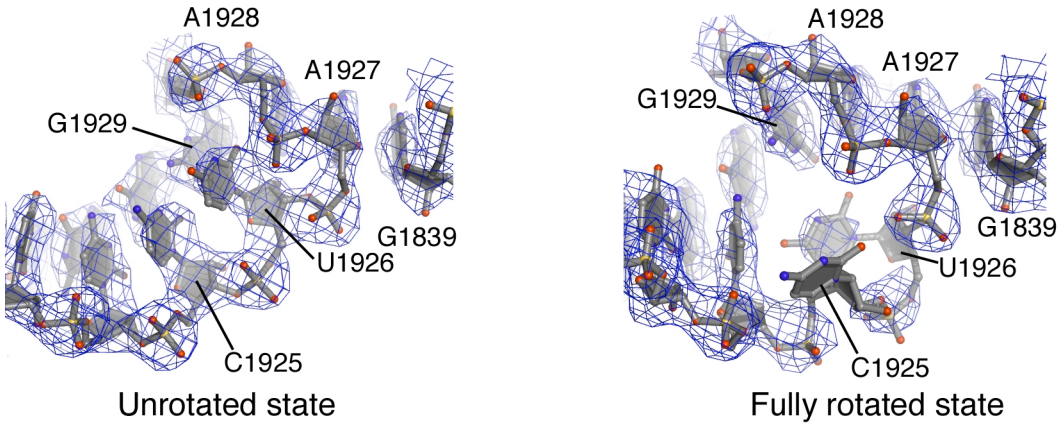

Figure S5. Extrusion of C1925 and U1926 due to helix H69 compression. The ($2F_{Obs} - F_{Calc}$) electron density map contoured at 1.3 standard deviations from the mean is also shown.

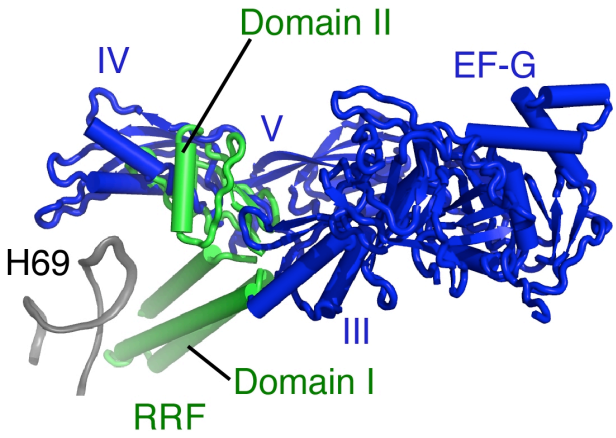

Figure S6. Superposition of a fully rotated ribosome in a pre-translocation complex mimic (*10*) with the recycling intermediate structure. Domains IV and V of EF-G (blue) and domain II of RRF (green) significantly overlap, with some overlap of domain III in EF-G and hinge region of RRF. Helix H69 in the recycling complex is also shown for reference. Superposition used the 50S subunit as a frame of reference (*37*).

Movie S1. An animation showing the changes in tRNA conformation during its transit through the ribosome. The tRNA models were as follows: A/T $tRNA^{Phe}$, homology model based on (*21*); A/A $tRNA^{Phe}$ from (*81*); A/P $tRNA^{Phe}$ based on (*82*); P/P $tRNA^{Phe}$ from the present structure; p/E tRNA from the present structure; and E/E $tRNA^{Phe}$ from (*81*). The sites of tRNA binding are also shown in cartoon form for each conformation in the animation.

Movie S2. An animation showing the changes in helix H69 in 23S rRNA during ratcheting. The surface of helix h44 in the 30S subunit (light blue), protein S12 (dark blue), mRNA and $tRNA^{Phe}$ moving from the P/P to P/E sites are also shown.

Table S1. X-ray crystallographic statistics

Space group	$P2_12_12_1$	
unit cell (*a*, *b*, *c* in Å)	211.67, 438.07, 613.42	
Resolution (Å)	70 – 3.0	
(high-resolution shell)*		(3.35-3.16)
R_{merge}†	19.4	(57.7)
I / σ (I)	7.4	(1.8)
Completeness (%)	83.5	(66.1)
Measurement redundancy	5.3	(3.3)
Unique reflections	938,380	(101,586)
No. crystals used	10	

*Data beyond the high-resolution shell in parenthesis was used for refinement and map calculation, and extend to an I / σ (I) of about 1. Data are 92.5% complete in the 3.9 Å – 3.6 Å resolution shell, and 99% complete in lower-resolution shells.

†All statistics not in parentheses include data over the whole reported resolution range.

Table S2. X-ray structure refinement

Resolution (Å)		40 – 3.0		
No. Reflections		938,304		
R_{free} Set		19,021		
R/R_{free} (%)*		20.2/26.1		
No. non-H Atoms		293,365		
R.m.s. deviations				
Bond lengths (Å)		0.013		
Bond angles (°)		1.39		
Mean ADP values ($Å^2$)†				
State R_0 70S	29.0			
State R_F 70S	24.6			
Validation statistics**				
		State R_0 70S		State R_F 70S
All-atom clashscore		44.1	56th percentile	38.5	68th percentile
Ramachandran outliers		9.2%	10th percentile	8.4%	12th percentile
Ribose pucker outliers		1.6%	73rd percentile	1.9%	70th percentile
Bond + angle outliers		0.63%		1.77%	

*Refinement in Phenix (*59*) with riding H atoms.

†Atomic displacement parameter values are reported as isotropic B-factors. B-factor model is 2 per residue, wxu weight set to 1.66.

**From MolProbity (*60*).

Table S3. Nucleotides used for superpositions of the yeast and *E. coli* ribosomes

E. coli 16S rRNA	Yeast 18S rRNA	*E. coli* 23S rRNA	Yeast 25S rRNA
12 – 18	7 – 13	213 – 266	57 – 110
53 – 63	49 – 59	319 – 342	208 – 231
108 – 120	92 – 104	622 – 636	700 – 714
240 – 250	309 – 319	963 – 989	1133 – 1159
254 – 287	325 – 358	1662 – 1711	1894 – 1943
332 – 375	404 – 447	1758 – 1799	2116 – 2157
386 – 397	457 – 468	1882 – 1902	2225 – 2245
513 – 542	560 – 589	1923 – 2002	2266 – 2345
573 – 588	620 – 635	2064 – 2093	2406 – 2435
660 – 810	871 – 1021	2225 – 2255	2593 – 2623
880 – 925	1104 – 1149	2290 – 2346	2659 – 2715
937 – 968	1162 – 1193	2436 – 2520	2805 – 2889
1218 – 1245	1451 – 1478		
1306 – 1320	1543 – 1557		
1324 – 1383	1561 – 1620		
1399 – 1405	1636 – 1642		
1479 – 1486	1742 – 1749		
1494 – 1530	1757 – 1793		

References and Notes

51. E. Cayama *et al.*, *Nucleic Acids Res* **28**, E64 (2000).

52. R. Junemann *et al.*, *Nucleic Acids Res* **24**, 907 (1996).

53. G. von Ehrenstein, K. M. Lawrence Grossman, in *Methods in Enzymology*. (Academic Press, 1967), vol. Volume 12, Part 1, pp. 588-596.

54. S. C. Blanchard, H. D. Kim, R. L. Gonzalez, Jr., J. D. Puglisi, S. Chu, *Proc Natl Acad Sci U S A* **101**, 12893 (2004).

55. J. B. Munro *et al.*, *Proc Natl Acad Sci U S A* **107**, 709 (2010).

56. R. Dave, D. S. Terry, J. B. Munro, S. C. Blanchard, *Biophys J* **96**, 2371 (2009).

57. G. Blaha *et al.*, *Methods Enzymol* **317**, 292 (2000).

58. W. Kabsch, *J. Appl. Cryst.* **26**, 795 (1993).

59. P. D. Adams *et al.*, *Acta Crystallogr D Biol Crystallogr* **66**, 213 (2010).

60. V. B. Chen *et al.*, *Acta Crystallogr D Biol Crystallogr* **66**, 12 (2010).

61. X. Wang *et al.*, *J Math Biol* **56**, 253 (2008).

62. J. M. Word *et al.*, *J Mol Biol* **285**, 1711 (1999).

63. J. S. Richardson *et al.*, *RNA* **14**, 465 (2008).

64. J. M. Word, S. C. Lovell, J. S. Richardson, D. C. Richardson, *J Mol Biol* **285**, 1735 (1999).

65. P. Emsley, B. Lohkamp, W. G. Scott, K. Cowtan, *Acta Crystallogr D Biol Crystallogr* **66**, 486 (2010).

66. I. W. Davis, W. B. Arendall, 3rd, D. C. Richardson, J. S. Richardson, *Structure* **14**, 265 (2006).

67. V. B. Chen, I. W. Davis, D. C. Richardson, *Protein Sci* **18**, 2403 (2009).

68. V. B. Chen, Duke University (2010).

69. T. A. Jones, J. Y. Zou, S. W. Cowan, Kjeldgaard, *Acta Crystallogr. A* **47**, 110 (1991).

70. W. Saenger, *Principles of Nucleic Acid Structure*. C. R. Cantor, Ed., Springer Advanced Texts in Chemistry (Springer-Verlag, New York, 1984), pp. 556.

71. K. Cowtan, *Acta Crystallogr D Biol Crystallogr* **56**, 1612 (2000).

72. M. M. Yusupov *et al.*, *Science* **292**, 883 (2001).

73. M. Laurberg *et al.*, *Nature* **454**, 852 (2008).

74. L. B. Jenner, N. Demeshkina, G. Yusupova, M. Yusupov, *Nat Struct Mol Biol* **17**, 555 (2010).

75. D. J. Klein, P. B. Moore, T. A. Steitz, *J Mol Biol* **340**, 141 (2004).

76. W. L. Delano, *The PyMOL User's Manual*. (Delano Scientific, San Carlos, CA, USA., 2002).

77. Uniprot, *Nucleic Acids Res* **38**, D142 (2010).

78. N. Echols, D. Milburn, M. Gerstein, *Nucleic Acids Res* **31**, 478 (2003).

79. A. T. Brünger *et al.*, *Acta Crystallogr. D Biol. Crystallogr.* **54**, 905 (1998).

80. J. B. Munro, R. B. Altman, C. S. Tung, K. Y. Sanbonmatsu, S. C. Blanchard, *EMBO J* **29**, 770 (2010).

81. L. Jenner, N. Demeshkina, G. Yusupova, M. Yusupov, *Nat Struct Mol Biol* **17**, 1072 (2010).

82. X. Agirrezabala *et al.*, *Mol Cell* **32**, 190 (2008).